Title

Real-Time Observation of Water-Soluble Mineral Precipitation in Aqueous Solution by In Situ High-Resolution Electron Microscopy

Journal

ACS Nano, 10(1)

ISSN

1936-0851

Authors

Yuk, Jong Min

Zhou, Qin

Chang, Jiyoung

et al.

Publication Date

2016-01-26

DOI

10.1021/acsnano.5b04064

Peer reviewed

ACSNANO www.acsnano.org

ARTICLE

Real-Time Observation of Water-Soluble Mineral Precipitation in Aqueous Solution by *In Situ* High-Resolution Electron Microscopy

Jong Min Yuk,[†,⊥,¶] Qin Zhou,[†,⊥,¶] Jiyoung Chang,[†,⊥,¶] Peter Ercius,[∥] A. Paul Alivisatos,[‡,§,⊥,¶] and Alex Zettl[*,†,⊥,¶]

[†]Department of Physics, [‡]Department of Chemistry, and [§]Department of Materials Science, University of California, Berkeley, California 94720, United States

[⊥]Materials Sciences Division and [∥]The National Center for Electron Microscopy, The Molecular Foundry, Lawrence Berkeley National Laboratory, Berkeley, California 94720, United States

[¶]Kavli Energy NanoScience Institute at the University of California, Berkeley, and the Lawrence Berkeley National Laboratory, Berkeley, California 94720, United States

Supporting Information

ABSTRACT: **The precipitation and dissolution of water-soluble minerals in aqueous systems is a familiar process occurring commonly in nature. Understanding mineral nucleation and growth during its precipitation is highly desirable, but past *in situ* techniques have suffered from limited spatial and temporal resolution. Here, by using *in situ* graphene liquid cell electron microscopy, mineral nucleation and growth processes are demonstrated in high spatial and temporal resolution. We precipitate the mineral thenardite (Na_2SO_4) from aqueous solution with electron-beam-induced radiolysis of water. We demonstrate that minerals nucleate with a two-dimensional island structure on the graphene surfaces. We further reveal that mineral grains grow by grain boundary migration and grain rotation. Our findings provide a direct observation of the dynamics of crystal growth from ionic solutions.**

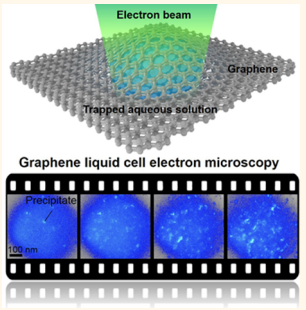

KEYWORDS: *in situ graphene liquid cell electron microscopy, water-soluble mineral, nucleation and growth, grain boundary migration, grain rotation*

The crystallization of dissolved salts in aqueous solution is involved in bio-, geo-, and soil mineralization and is the most common way of producing crystals in nature.[1−3] A fundamental understanding of crystallization from solution is necessary to control and optimize crystal structure, morphology, and the size of the products. The key steps affecting the final structures and properties are the crystal nucleation and subsequent growth.[4−6] Despite great interest in this pathway, the pathways of crystallization are still ambiguous because processes that occur in liquid are difficult to access with current experimental methods. While an aqueous environment presents many challenges to experimental investigation, grazing-incidence small-angle X-ray scattering (GISAXS), atomic force microscopy (AFM), and optical microscopy have previously been employed to obtain dynamical information on mineral nucleation and growth, such as calcium carbonate, iron oxide, sodium chloride, and silica.[7−10] Using these *in situ* methods, it has been demonstrated that, depending on the supersaturation, precipitation occurs predominantly by attaching molecules at screw dislocations or through two-dimensional (2D) surface nucleation.[4−6] However, these experimental methods have their limitations. For example, *in situ* spectroscopy methods cannot provide morphological information, and *in situ* AFM can be applied only for fixed samples on a substrate with limited temporal resolution, constraining the utility in colloidal synthesis investigation.

Liquid cell transmission electron microscopy (TEM) provides unique advantages, by allowing direct observation of the morphological and structural changes of particles in solution during chemical and physical reactions. This method has been employed for the observation of nucleation and growth of colloidal nanocrystals.[10−16] Since mineral precipitation by water evaporation is technically difficult to achieve in a TEM, application of *in situ* liquid cell TEM has been limited to the experiments initiated by electron-beam-induced reduction of metal ions.[10−16] In this article, we not only introduce the mineral precipitation by electron-beam-induced radiolysis of water instead of water evaporation occurring in nature but also show the precipitation processes of the mineral

Received: July 2, 2015
Accepted: December 3, 2015

DOI: 10.1021/acsnano.5b04064
ACS Nano XXXX, XXX, XXX−XXX

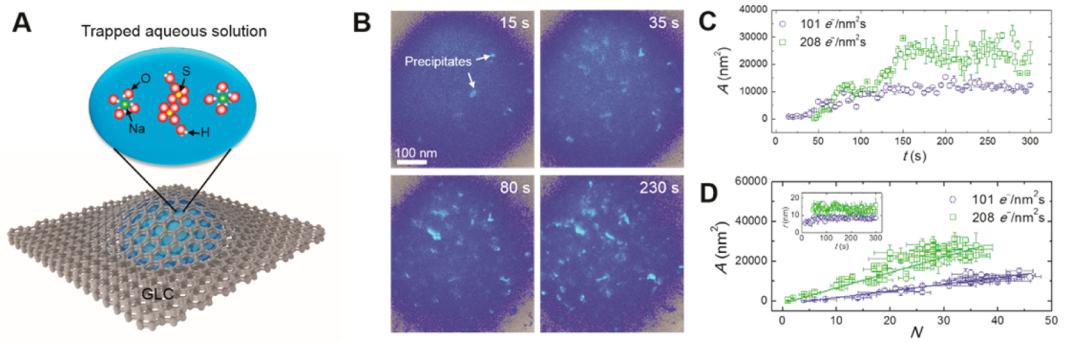

Figure 1. Time-lapse TEM imaging of mineral nucleation from aqueous solution. (A) Schematic of the GLC with sodium persulfate aqueous solution trapped between FLG sheets. Sodium and persulfate ions are solvated by water molecules. (B) Time-lapse, color-contrasted, dark-field TEM images of mineral precipitation by electron beam irradiation. (C) Total projected area (A) of all precipitates *versus* electron beam irradiation time (t). (D) A *versus* the number of precipitates (N). Inset, mean radius (r) of precipitates *versus* t. Line in (d) indicates the linear fitting.

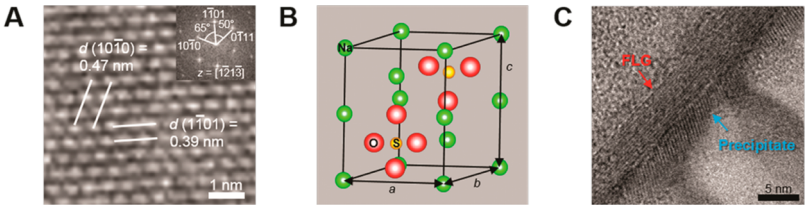

Figure 2. HR-TEM imaging of the sodium sulfate nucleus. (A) HR-TEM image of hexagonal sodium sulfate mineral with $[1\bar{2}1\bar{3}]$ zone axis. Inset is the FFT image of (A). (B) Structure of hexagonal sodium sulfate crystal ($a = b = 0.54$ nm and $c = 0.72$ nm). (C) HR-TEM image of the sodium sulfate nucleus with thickness less than 5 nm deposited on the FLG with ~12 layers.

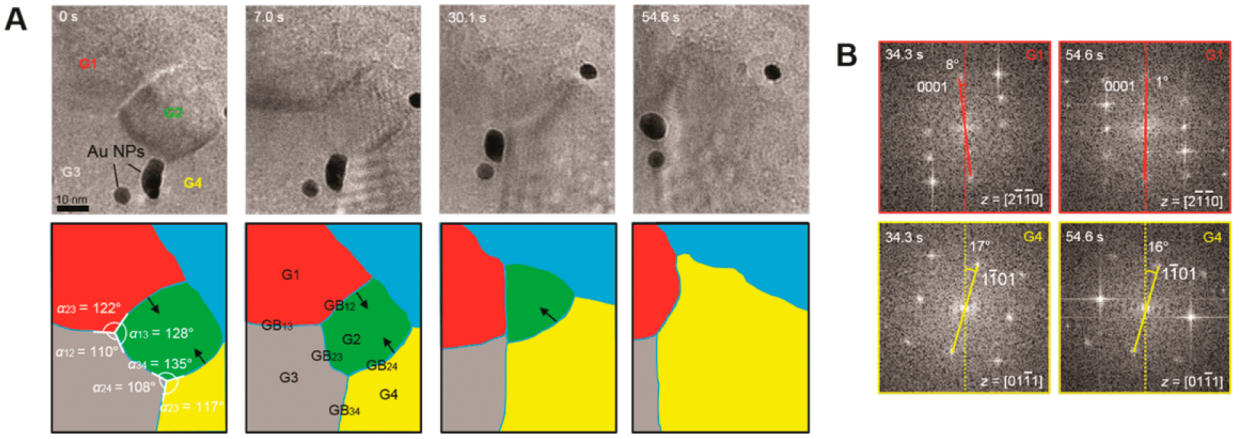

Figure 3. HR-TEM imaging of mineral grain growth by the grain boundary migration and the grain rotation. (A) Time-serial HR-TEM images (top row of images) and the corresponding false-colored schematics identifying grains and grain boundaries (bottom row of images). At 0 s, the precipitate is composed of four crystalline grains of G1, G2, G3, and G4 and five grain boundaries of GB_{12}, GB_{13}, GB_{23}, GB_{24}, and GB_{34}. α_{23}, α_{13}, and α_{12} of the angles between grain boundaries are 122, 128, and 110°, respectively. Au particles are loaded as an indicator of liquid environment. Due to the migration of GB_{12} and GB_{24} toward center of curvature, the G2 changes shape, which assumes a planar rectangular shape at 7.0 s and a triangular shape at 30.1 s, and eventually disappears at 54.6 s. In the schematics at 0, 7.0, and 30.1 s, arrows indicate the directions of grain boundary migration. (B) (0001) diffraction spot of G1 rotates relative to vertical lines by 8 and 1° at 34.3 and 54.6 s, respectively. (1$\bar{1}$01) diffraction spot of G4 rotates relative to vertical lines by 17 and 16° at 34.3 and 54.6 s, respectively.

thenardite (Na_2SO_4), which is used in the glass, paper, and medical industries.[17]

RESULTS AND DISCUSSION

For observation of mineral precipitation in high spatial and temporal resolution, we employ graphene liquid cells (GLCs) in a TEM to achieve high contrast imaging of the target materials in solution.[13,18,19] Figure 1A shows a schematic of the GLC composed of two few-layer graphene (FLG) sheets (2–15 layers in Figure S1A) trapping sodium persulfate aqueous solution (Figure S1B), in which the sodium and persulfate ions are solvated by water molecules. We prepare the GLCs on Quantifoil gold TEM grids using a method that directly encapsulates a target solution between free-standing FLG sheets (see Methods and Figure S2). This method can increase the yield of graphene pockets (Figure S3), compared to a previous method using monolayer graphene sheets,[13] and can be directly adaptable to the liquid cell fabrication with

DOI: 10.1021/acsnano.5b04064
ACS Nano XXXX, XXX, XXX−XXX

biological samples.[20] The addition of a few graphene sheets has minimal impact on TEM resolution compared to the impact of the liquid itself.

Since sodium sulfate nanocrystals are indiscernible in bright-field TEM images due to their low mass−thickness contrast, to observe the mineral nucleation,[21] we acquire time-lapse dark-field TEM images by choosing the precipitates' diffraction spots with an objective aperture (Figures 1B and S4 and Movies S1 and S2). Initially, sodium persulfate salts are totally dissolved in water, which is indicated by the halo feature in the diffraction pattern (Figure S5 and Movie S3). Once the electron beam irradiation begins, minerals precipitate and nucleate. The diffraction spots of the precipitates correspond to sodium sulfate crystals (PDF #27-0791) (Figure S5). Figure 1C shows the total projected areas of the mineral precipitates as a function of the electron beam irradiation time. The amount of precipitates increases with the electron beam irradiation time because the water is depleted by the electron beam radiolysis. Although the mean radius ($r = (S/\pi)^{1/2}$, where S is the projected area of each precipitate) of the precipitates is constant (7.5 and 13.2 nm at 101 and 208 e^-/nm^2 s, respectively, in the inset of Figure 1D), the total projected areas of all precipitates increase linearly with the number of precipitates (Figure 1D). This indicates that mineral nuclei spread during electron beam irradiation. Mineral precipitation by the spread of nuclei is known to occur in a highly supersaturated solution using conventional synthesis methods.[4−6]

To investigate the structure of the mineral nuclei, we observe a single mineral nucleus at high resolution. Although sodium, sulfur, and oxygen atoms are relatively light atoms, Figure 2A shows a clear high-resolution TEM (HR-TEM) image, and the corresponding fast Fourier transformation (FFT) image (Figure S6) shows the hexagonal structure of the sodium sulfate crystal (Figure 2B). Figure 2C shows a HR-TEM image of the precipitates on the FLG edge. It indicates that sodium sulfate nanocrystals nucleate on graphene surfaces to lower the interfacial energy,[1,9] which also occurs in the conventional SiN liquid cell.[22] The 2D shape of the nuclei has a small thickness of less than 5 nm (Figure S4), which is formed in a high supersaturated solution using conventional synthesis methods.[4−6]

We monitor real-time mineral grain growth in the aqueous solution. Figure 3A shows time-serial HR-TEM images of grain boundary migration (Movie S4). The motion of the gold nanoparticles indicates that there is a liquid environment. Initially, the precipitate consists of four grains G1, G2, G3, and G4 with different crystallographic orientations (Figure S7) and five grain boundaries (GB_{12}, GB_{24}, GB_{13}, GB_{23}, and GB_{34}). In the aqueous solution, water molecules can be structurally incorporated in mineral grain boundaries with a highly disordered lattice. In the grain boundaries incorporating water molecules, unstable adatoms in convex surfaces dissolve and reprecipitate on concave surfaces (Figure S8), and hence the grain boundaries migrate,[22−26] which does not occur in a dried environment (Figure S9). When the grain boundaries are mobile, at a triple junction where G1, G2, and G3 meet, a local mechanical equilibrium is established and the requirement for equilibrium is $(\gamma_{12}/\sin\alpha_3) = (\gamma_{13}/\sin\alpha_2) = (\gamma_{23}/\sin\alpha_1)$,[22] where γ_{12}, γ_{13}, and γ_{23} are the relative boundary energies of the GB_{12}, GB_{13}, and GB_{23}, respectively, and α_1, α_2, and α_3 are the angles between GB_{12} and GB_{13}, GB_{12} and GB_{23}, and GB_{13} and GB_{23}, respectively. Since $\sin\alpha_3$ is larger than $\sin\alpha_1$ and $\sin\alpha_2$ at 0 s, γ_{12} should be relatively higher than γ_{23} and γ_{13}. Thus, the GB_{12} migrates toward the center of curvature to reduce the γ_{12}.[22−26] The GB_{24} also migrates for the same reason. At 30.1 s, the migration of GB_{12} and GB_{24} leads to the formation of a three-sided G2, and GB_{12} stops migration when GB_{12} is mechanically stabilized by GB_{34}. At 54.6 s, the G2 eventually disappears due to the migration of curved GB_{24}. It is noted that the migration speeds of grain boundaries are similar to or without gold particles, indicating that the gold particles do not affect the grain growth of minerals.

Figure 3B shows the FFTs corresponding to HR-TEM images of G1 and G4 during grain growth. For 10.3 s, G1 and G4 rotate 7 and 1°, respectively, which indicates that grains rotate separately during grain growth. In nature, grain boundary migration and grain rotation occur in aqueous solution to reduce the energy of dislocations, point defects, and grain boundaries.[22−26]

Figure 4A−D shows the schematics representing a proposed mineral precipitation mechanism by electron beam irradiation. The sodium and persulfate ions are initially solvated by water molecules (Figure 4A), and electron beam irradiation yields spurs, spaced according to the electrons' mean free path (Figure 4B).[16] In the spurs, water molecules are excited or ionized, producing radicals, ions, and molecular species such as e_h (the hydrated electron), H_3O^+, $\dot{H}$, $O\dot{H}$, H_2, O_2, and H_2O_2.[16] Radiolytic H_2 and O_2 contribute to the formation of bubbles (Figure S10).[16] By electron beam radiolysis in the spurs, sodium and persulfate ions are dehydrated and persulfate ions decompose to sulfate ions.[27−29] In the undersaturated solution, dehydrated sodium and sulfate ions are solvated again by water molecules. As the electron beam dose accumulates, the amount of water decreases and hence mineral ions become saturated in solution. When mineral ions are supersaturated, clusters of dehydrated mineral ions are generated in the spurs and form stable nuclei (Figure 4C). Under continuous electron beam irradiation, the nuclei spread out and grains grow by grain boundary migration and grain rotation (Figure 4D).

CONCLUSION

In conclusion, we present a new *in situ* approach for high-resolution imaging of mineral precipitation using the GLC-TEM method. We show nucleation and growth processes of sodium sulfate, which is difficult to achieve with traditional thick SiN liquid cells because sodium sulfate crystals are thin and composed of light atoms. Since graphene is a relatively chemically inert semimetal, the graphene windows of our cell are not expected to appreciably influence the charge distribution and spur formation in solution other than to confine it to a small volume. Our findings faithfully mimic mineral precipitation processes occurring in nature, such as mineral nucleation and mineral grain growth in highly supersaturated solution. This work goes beyond the specific material system studied here or methodology applied here and hence will likely benefit precipitation studies of many different naturally occurring minerals, such as calcium carbonate and sodium chloride.

METHODS

GLC Fabrication. FLG sheets were synthesized on Cu foil (99.8% Alfa Aesar, Ward Hill, MA) with flowing 200 sccm H_2 and 18 sccm CH_4 gas at 1050 °C for 1 h using atmospheric pressure chemical vapor deposition.[30] After the supporting Cu foil was etched away with a $Na_2S_2O_8$ solution (concentration of 0.1 g of $Na_2S_2O_8$/1 mL of water)

DOI: 10.1021/acsnano.5b04064
ACS Nano XXXX, XXX, XXX−XXX

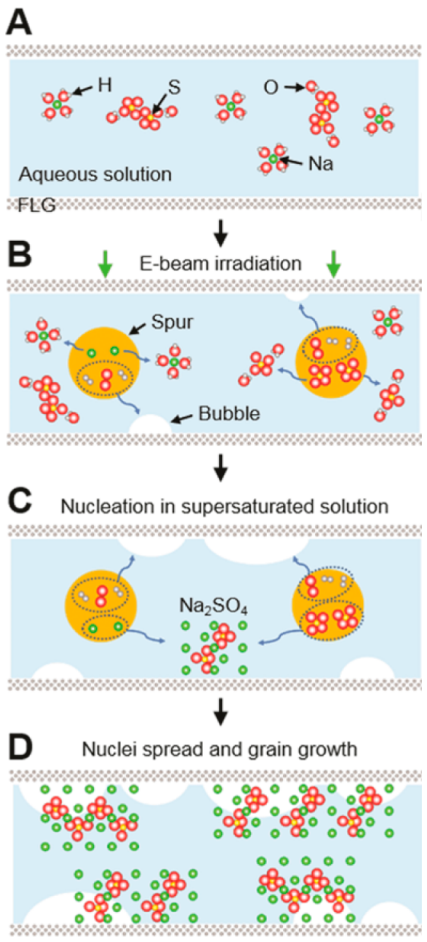

Figure 4. Schematics representing proposed precipitation processes of sodium sulfate minerals by electron beam radiolysis of water. (A) Initially, sodium and persulfate ions are solvated by water molecules. (B) Immediately after the electron beam irradiation, water molecules are excited or ionized in the spurs created along electron paths, resulting in dehydration of sodium and persulfate ions, creation of bubbles composed of H_2 and O_2, and decomposition of the persulfate ions to sulfate ions. In the undersaturated solution, dehydrated sodium and sulfate ions are solvated again by water molecules. As water is decomposed by continuous electron beam irradiation, mineral ions become saturated in solution. (C) When mineral ions are supersaturated, sodium sulfate nanocrystals nucleate on graphene surfaces. (D) Under continuous electron beam irradiation, the nuclei spread out and grains grow by grain boundary migration and grain rotation.

overnight (Figure S2A), the FLG sheet was rinsed with deionized water (Figure S2B). The free-floating FLG sheet was intact without any supporting substrates and clearly visible optically under normal illumination condition (see optical image in Figure S2B), while a single graphene sheet was visible optically by using evanescent waves due to its negligible reflectance.[20] The FLG sheet was moved to target aqueous solution (Figure S2C), which was prepared by dissolving $Na_2S_2O_8$ (Sigma-Aldrich, powder form, ≥98%) salts in water (0.43 M/L), followed by scooping up the FLG and the target solution with first transferred FLG on TEM grids (Figure S2D). The solution was eventually trapped between two FLG sheets (Figure S2E), which was sealed *via* a van der Waals interaction where the solution was removed.[13,31] In the samples for HR-TEM imaging, Au nanoparticles (Sigma-Aldrich, 5 nm diameter) were mixed in the target solution as an indicator of a liquid environment.

TEM Imaging and Spectroscopy. Bright- and dark-field TEM images and diffraction patterns were acquired using a JEM-2010 LaB_6 instrument (JEOL Ltd.) at 80 kV. Dark-field TEM imaging was performed by selecting diffracted spots from precipitates in diffraction mode with a 0.5 nm^{-1} objective aperture. HR-TEM imaging was conducted with the TEAM 1 operated at 80 kV at the Molecular Foundry. Energy-disperse X-ray spectroscopy was performed in the diffraction mode using an Oxford INCA energy-dispersive X-ray detector, installed in the Philips CM200/FEG operated at 200 kV at the Molecular Foundry.

ASSOCIATED CONTENT

Supporting Information

The Supporting Information is available free of charge on the ACS Publications website at DOI: 10.1021/acsnano.5b04064.

Additional figures and movie descriptions (PDF)
Movie 1 (AVI)
Movie 2 (AVI)
Movie 3 (AVI)
Movie 4 (AVI)

AUTHOR INFORMATION

Corresponding Author

*E-mail: azettl@berkeley.edu.

Notes

The authors declare no competing financial interest.

ACKNOWLEDGMENTS

We thank C. Song at the Molecular Foundry for experimental assistance with TEM, and S. Nguyen at U.C. Berkeley for helpful discussions. J.M.Y., Q.Z., J.C., and A.Z. acknowledge support from the Director, Office of Energy Research, Basic Energy Sciences, Materials Sciences and Engineering Division, of the U.S. Department of Energy under Contract DE-AC02-05CH11231 within the SP2-Bonded Materials Program and The Molecular Foundry, which provided for construction of the GLC and TEM characterization, respectively; the Office of Naval Research under Grant N00014-12-1, which provided for graphene growth; the NSF under Grant DMR-1206512, which provided for development of graphene transfer methods; and DTRA Grant HDTRA1-13-1-0035, which provided postdoctoral support.

REFERENCES

(1) De Yoreo, J. J.; Vekilov, P. G. Principles of Crystal Nucleation and Growth. *Rev. Mineral. Geochem.* **2003**, *54*, 57−93.
(2) Special Issue on Crystal Growth and Nucleation. *Faraday Discuss.* **2007**, *136*, 1−426.
(3) Anwar, J.; Zahn, D. Uncovering Molecular Processes in Crystal Nucleation and Growth by Using Molecular Simulation. *Angew. Chem., Int. Ed.* **2011**, *50*, 1996−2013.
(4) Land, T. A.; De Yoreo, J. J.; Lee, J. D. An *In-Situ* AFM Investigation of Canavalin Crystallization Kinetics. *Surf. Sci.* **1997**, *384*, 136−155.
(5) Land, T. A.; De Yoreo, J. J. The Evolution of Growth Modes and Activity of Growth Sources on Canavalin Investigated by *In Situ* Atomic Force Microscopy. *J. Cryst. Growth* **2000**, *208*, 623−637.
(6) Teng, H. H.; Dove, P. M.; De Yoreo, J. J. Kinetics of Calcite Growth: Surface Processes and Relationships to Macroscopic Rate Laws. *Geochim. Cosmochim. Acta* **2000**, *64*, 2255−2266.
(7) Teng, H. H.; Dove, P. M.; Orme, C. A.; De Yoreo, J. J. Thermodynamics of Calcite Growth: Baseline for Understanding Biomineral Formation. *Science* **1998**, *282*, 724−727.
(8) Davis, K. J.; Dove, P. M.; De Yoreo, J. J. The Role of Mg^{2+} as an Impurity in Calcite Growth. *Science* **2000**, *290*, 1134−1137.

DOI: 10.1021/acsnano.5b04064
ACS Nano XXXX, XXX, XXX−XXX

(9) De Yoreo, J. J.; Waychunas, G. A.; Jun, Y. − S.; Fernandez-Martinez, A. *In situ* Investigations of Carbonate Nucleation on Mineral and Organic Surfaces. *Rev. Mineral. Geochem.* **2013**, *77*, 229−257.
(10) Desarnaud, J.; Derluyn, H.; Carmeliet, J.; Bonn, D.; Shahidzadeh, N. Metastability Limit for the Nucleation of NaCl Crystals in Confinement. *J. Phys. Chem. Lett.* **2014**, *5*, 890−895.
(11) Zheng, H.; Smith, R. K.; Jun, Y. − W.; Kisielowski, C.; Dahmen, U.; Alivisatos, A. P. Observation of Single Colloidal Platinum Nanocrystal Growth Trajectories. *Science* **2009**, *324*, 1309−1312.
(12) Woehl, T. J.; Evans, J. E.; Arslan, I.; Ristenpart, W. D.; Browning, N. D. Direct *In Situ* Determination of the Mechanisms Controlling Nanoparticle Nucleation and Growth. *ACS Nano* **2012**, *6*, 8599−8610.
(13) Yuk, J. M.; Park, J.; Ercius, P.; Kim, K.; Hellebusch, D. J.; Crommie, M. F.; Lee, J. Y.; Zettl, A.; Alivisatos, A. P. High-Resolution EM of Colloidal Nanocrystal Growth Using Graphene Liquid Cells. *Science* **2012**, *336*, 61−64.
(14) Uematsu, T.; Baba, M.; Oshima, Y.; Tsuda, T.; Torimoto, T.; Kuwabata, S. Atomic Resolution Imaging of Gold Nanoparticle Generation and Growth in Ionic Liquids. *J. Am. Chem. Soc.* **2014**, *136*, 13789−13797.
(15) Liao, H. − G.; Zherebetskyy, D.; Xin, H.; Czarnik, C.; Ercius, P.; Elmlund, H.; Pan, M.; Wang, L. − W.; Zheng, H. Facet Development during Platinum Nanocube Growth. *Science* **2014**, *345*, 916−919.
(16) Grogan, J. M.; Schneider, N. M.; Ross, F. M.; Bau, H. H. Bubble and Pattern Formation in Liquid Induced by an Electron Beam. *Nano Lett.* **2014**, *14*, 359−364.
(17) Cocchetto, D. M.; Levy, G. Absorption of Orally Administered Sodium Sulfate in Humans. *J. Pharm. Sci.* **1981**, *70*, 331−333.
(18) Yuk, J. M.; Seo, H. K.; Choi, J. W.; Lee, J. Y. Anisotropic Lithiation Onset in Silicon Nanoparticle Anode Revealed by *In Situ* Graphene Liquid Cell Electron Microscopy. *ACS Nano* **2014**, *8*, 7478−7485.
(19) Chen, Q.; Smith, J. M.; Park, J.; Kim, K.; Ho, D.; Rasool, H. I.; Zettl, A.; Alivisatos, A. P. 3D Motion of DNA-Au Nanoconjugates in Graphene Liquid Cell Electron Microscopy. *Nano Lett.* **2013**, *13*, 4556−4561.
(20) Wang, C.; Qiao, Q.; Shokuhfar, T.; Klie, R. F. High-Resolution Electron Microscopy and Spectroscopy of Ferritin in Biocompatible Graphene Liquid Cells and Graphene Sandwiches. *Adv. Mater.* **2014**, *26*, 3410−3414.
(21) Smeets, P. J. M.; Cho, K. R.; Kempen, R. G. E.; Sommerdijk, N. A. J. M.; De Yoreo, J. J. Calcium Carbonate Nucleation Driven by Ion Binding in a Biomimetic Matrix Revealed by *In Situ* Electron Microscopy. *Nat. Mater.* **2015**, *14*, 394−399.
(22) Schenk, O.; Urai, J. L.; Piazolo, S. Structure of Grain Boundaries in Wet, Synthetic Polycrystalline, Statically Recrystallizing Halite−Evidence from Cryo-SEM Observations. *Geofluids* **2006**, *6*, 93−104.
(23) Schenk, O.; Urai, J. L. Microstructural Evolution and Grain Boundary Structure during Static Recrystallization in Synthetic Polycrystals of Sodium Chloride Containing Saturated Brine. *Contrib. Mineral. Petrol.* **2004**, *146*, 671−682.
(24) Lehner, F. K. *Deformation Processes in Minerals, Ceramics and Rocks*; Springer: The Netherlands, 1990; pp 296−333.
(25) Drury, M. R.; Urai, J. L. Deformation-Related Recrystallization Processes. *Tectonophysics* **1990**, *172*, 235−253.
(26) Rubie, D. C. The Catalysis of Mineral Reactions by Water and Restrictions on the Presence of Aqueous Fluid during Metamorphism. *Mineral. Mag.* **1986**, *50*, 399−415.
(27) Evans, J. E.; Jungjohann, K. L.; Browning, N. D.; Arslan, I. Controlled Growth of Nanoparticles from Solution with *In Situ* Liquid Transmission Electron Microscopy. *Nano Lett.* **2011**, *11*, 2809−2813.
(28) Kolthoff, I. M.; Miller, I. K. The Chemistry of Persulfate. I. The Kinetics and Mechanism of the Decomposition of the Persulfate Ion in Aqueous Medium. *J. Am. Chem. Soc.* **1951**, *73*, 3055−3059.
(29) Criquet, J.; Leitner, N. K. V. Degradation of Acetic Acid with Sulfate Radical Generated by Persulfate Ions Photolysis. *Chemosphere* **2009**, *77*, 194−200.
(30) Bhaviripudi, S.; Jia, X.; Dresselhaus, M. S.; Kong, J. Role of Kinetic Factors in Chemical Vapor Deposition Synthesis of Uniform Large Area Graphene Using Copper Catalyst. *Nano Lett.* **2010**, *10*, 4128−4133.
(31) Yuk, J. M.; Kim, K.; Alemán, B.; Regan, W.; Ryu, J. H.; Park, J.; Ercius, P.; Lee, H. M.; Alivisatos, A. P.; Crommie, M. F.; et al. Graphene Veils and Sandwiches. *Nano Lett.* **2011**, *11*, 3290−3294.

DOI: 10.1021/acsnano.5b04064
ACS Nano XXXX, XXX, XXX−XXX